DOI 10.1007/s10946-017-9676-y
Journal of Russian Laser Research, Volume 38, Number 6, November, 2017

COHERENT PHONON-MODE EXCITATION IN SUBMICRON SINGLE-CRYSTAL DIAMOND FILMS WITH A GRAPHITIZED LAYER BUILT-IN

M. V. Tareeva,[1*] V. A. Dravin,[1] R. A. Khmelnitsky,[1,2,3,4] A. D. Kudryavtseva,[1] M. A. Strokov,[1] M. A. Shevchenko,[1] N. V. Tcherniega,[1] and K. A. Tsarik[5]

[1] *Lebedev Physical Institute, Russian Academy of Sciences*
Leninskii Prospect 53, Moscow 119991, Russia

[2] *Kotel'nikov Institute of Radio Engineering and Electronics, Russian Academy of Sciences*
Fryazino Branch, Fryazino, Moscow Region 141190, Russia

[3] *Prokhorov General Physics Institute, Russian Academy of Sciences*
Vavilova Street 38, Moscow 119991, Russia

[4] *Troitsk Institute for Innovation and Fusion Research (GNTs RF TRINITI)*
Pushkovykx Street 12, Troitsk, Moscow 142190, Russia

[5] *National Research University of Electronic Technology*
Shokin Square 1, Zelenograd, Moscow 124498, Russia

[*] Corresponding author e-mail: tareeva@sci.lebedev.ru

Abstract

We report the first experimental observation of high-efficient phonon-mode coherent excitation using stimulated low-frequency Raman scattering (SLFRS) in submicron diamond–graphite–diamond heterostructure films with an ion-beam-induced graphitized layer. We show that the SLFRS process in submicron diamond heterostructures has a frequency shift in the gigahertz range and estimate experimentally the SLFRS conversion efficiency and threshold.

Keywords: phonon-mode excitation, stimulated low-frequency Raman scattering, ion-implanted diamond, graphitized layer.

1. Introduction

Rapid development of technologies based on tunable lasers [1] demands discovery of new nonlinear optical materials for coherent generation of electromagnetic waves in the infrared and terahertz ranges [2]. It is well known that the efficiency of nonlinear processes in crystals increases with the input power but, at the same time, it is limited by low laser-damage thresholds of such crystals [3]. Higher damage thresholds and conversion efficiencies can be obtained by coating the crystals with appropriate films [4].

Extendedly high thermal conductivity and thermal stress parameters of diamond make this material tolerant to laser damage [5]; it is one of the best candidates for efficient nonlinear generation. For this reason and due to optical transparency, thermal and environmental stability, and other complimentary characteristics that are orders of magnitude higher than those in other laser materials, diamond films are actively used for optical windows [6] as well for a variety of optical coatings [7] and surface acoustic wave devices [8].

Manuscript submitted by the authors in English on October 26, 2017.

 1071-2836/17/3806-0530

The importance of diamond for nonlinear optics is hardly overestimated. Unique physical properties of single-crystal diamond make this structure an irreplaceable material in optoelectronic circuits and micro- and nano-electromechanical systems (see, e.g., [9,10]). Biocompatible diamond-based platforms are intensively developed for the controlled delivery of different therapeutic compounds and other applications in biology and nanoscale medicine [11].

Using a basic design strategy, synthetic diamonds can be employed as nano-mechanical resonators, optical waveguides, and microdisk cavities [10, 12]. Continuous progress in diamond synthesis [13, 14] has made possible many achievements in nanophotonics and quantum information processing [15, 16]. Ion implantation in combination with high-temperature annealing is used in the lift-off technique to obtain free-standing diamond plates with opto-acoustic and thermo-conductive characteristics that are specific for bulk single crystals [13, 17, 18].

Nowadays, the challenge in diamond technology is high-quality free-standing ultrathin diamond films [16] and their integration into complex systems [6, 10, 13, 15]. Fragile ultrathin 30–100 nm membranes are hardly operated independently of the substrate. At the same time, in the case of comparable thicknesses of the Raman active media and wavelengths of pumping laser radiation, it is reasonable to expect efficient Raman generation and photon up-conversion. From the experimental point of view, treatment of submicron SCD membranes is a question of compromise between high laser-damage thresholds and short lengths of interaction.

The other problem is unavoidable defects in synthetic diamonds [19], which necessarily change the picture of subsurface stress distribution and subsequently affect Raman scattering and luminescent spectra, as well as the refractive index of synthesized samples [20]. Nevertheless, recently observed stimulated Raman scattering (SRS) in CVD diamonds [21] attests to the great potential of synthetic diamonds for nonlinear optics. This success shows the necessity of further investigations of diamond thin films in the pursuit of a highly-efficient second-order nonlinearity.

In this paper, we present a method to utilize ultra-thin SCD films for effective nonlinear scattering in the stimulated regime in a nondestructive manner using all the advantages of extremely high Young's modulus together with a relatively wide Raman frequency shift and high values of the refractive index and thermal conductivity of diamond. As proof of concept, we use the methodology elaborated for effective generation of acoustic modes and stimulated Raman scattering in submicron SCD films restored in diamond–graphite–diamond heterostructures.

As is well known, low-frequency Raman scattering is employed as an effective method for studying nanoscaled systems, since it has been experimentally observed for the first time in the spontaneous regime [22]. The SLFRS, in contrast to the SRS, is a result of light interaction with nanoscale systems; its frequency shifts are much smaller than that for SRS and lie in the gigahertz and terahertz ranges [23–26].

2. Preparation and Characterization of Samples

2.1. Preparation of Samples

As the initial samples for ion implantation and annealing, we used polished plates of natural diamond with nitrogen impurity content less than $5 \cdot 10^{18}$ cm^{-3}. The diamond samples were cut from natural single crystals parallel to the {110} crystallographic plane (see Fig. 1). There is anisotropy of elastic modulus in the diamond in these directions. Some nonlinear properties of natural diamond $^{\mathrm{nat}}$C are presented in the Table 1.

Table 1. Some Physical Properties and Nonlinear Characteristics of Diamond of Natural Isotopic Composition ^{nat}C at Room Temperature and $\lambda = 0.6943$ μm.

Physical characteristics	Value	Reference
Biaxial elastic moduli, GPa	$M_{100} = 1170$ $M_{110} = 1320$	[27]
Longitudinal (l) and transverse (t) wave velocity, km/s	$v^l_{100} = 17.5$ $v^{t1}_{100} = v^{t2}_{100} = v^{t1}_{110} = 12.8$ $v^l_{110} = 18.3$, $v^{t2}_{110} = 11.6$	[28]
Nonlinearity type	$\chi^{(3)}$	[3]
Frequency of the SRS-active mode, cm^{-1}	$\Delta\omega_{SRS} \sim 1332.5 \pm 0.5$	[29]
Refractive index (Sellmeier equation)	$n \approx 2.435$	[30]
Raman linewidth, cm^{-1}	2.04	[31]*
SRS generation threshold, $GW \cdot cm^{-2}$	1.2	[31]
Constant energy transmission coefficient threshold, $GW \cdot cm^{-2}$	< 3.6 (at 0.532 μm)	[3]
Raman gain coefficient, $cm \cdot GW^{-1}$	$g_{\langle 110\rangle} = 6.9$	[31]
Two-photon absorption coefficient, $cm \cdot GW^{-1}$	< 0.26 (at 0.53 μm)	[3]
Laser damage threshold, $J \cdot cm^{-2}$	$\sim 65 - 95$ (at 1.064 μm)	[32]*
Breakdown field, $MV \cdot cm^{-1}$	> 10	[5]

*For type IIa diamond.

A thin submicron ion-beam-induced graphitized layer was fabricated in each sample of submicron SCD film (see Fig. 1, where we present a schematic profile view of typical diamond–graphite–diamond heterostructure used in our experiment).

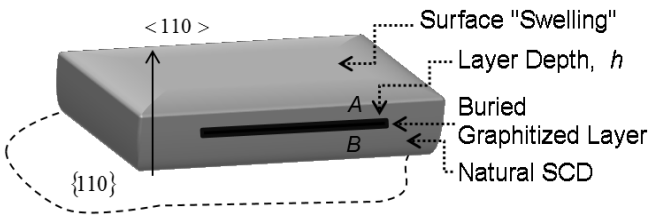

Fig. 1. Schematic image (profile view) of SCD films with ion-beam-induced graphitized layer. The graphitized layer is buried on depth h (see Table 2) and has boundaries with roughness of about 7 nm (A and B) with a bulk SCD (thickness 300 μm). Surface swelling ranges from 20 to 100 nm in different samples.

Buried graphitized layers were fabricated in bulk natural diamond by light ion implantation. Ion implantation always leads to the radiation damage of material, so annealing of heavily damaged diamond leads to the formation of a graphitized layer in the region of maximum radiation damage, in which carbon atoms are bound by sp^2 bonds [33]. As a result of such treatment, the graphitized layer is covered by restored submicron single-crystal diamond [34]. For radiation damage, the polished samples have been bombarded at room temperature by $^{12}C^+$, $^4He^+$ ions with energy 50–350 keV (see Table 2).

All implanted samples have been annealed for 1 h at temperatures 1,480 °C in vacuum at 10^{-3} Pa in a graphite wall furnace. The thin graphite surface layer (as thin as 1 nm according to optical absorption data) that appeared after high-vacuum annealing was etched out in a $H_2SO_4 + K_2Cr_2O_7$ solution at a temperature of about 180 °C.

Table 2. Ion Implantation Regimes for Pristine Samples of Natural Diamonds and Parameters of Buried Graphitized Layer Calculated by the Monte Carlo Technique.

Sample name	Type of ion	Ion energy keV	Annealing temperature °C	Implantation dose 10^{16} cm^{-2}	Restored SCD layer depth h, nm	Graphitized layer thickness nm
#1	$^4He^+$	180	1480	4	450	80
#2	$^4He^+$	50	1480	2.5	185	84
#3	$^{12+}$	350	1480	0.4	365	100

2.2. Depth of Graphitization Layer

The actual thickness of the restored diamond layer covering the graphitized layer was defined by the depth of the buried graphitized layer in a bulk material and controlled by type, energy of bombarding ions, and implantation dose. We estimated the position and thickness of the graphitized layer considering the level of radiation damage distributed in the profile of the sample (see Fig. 2).

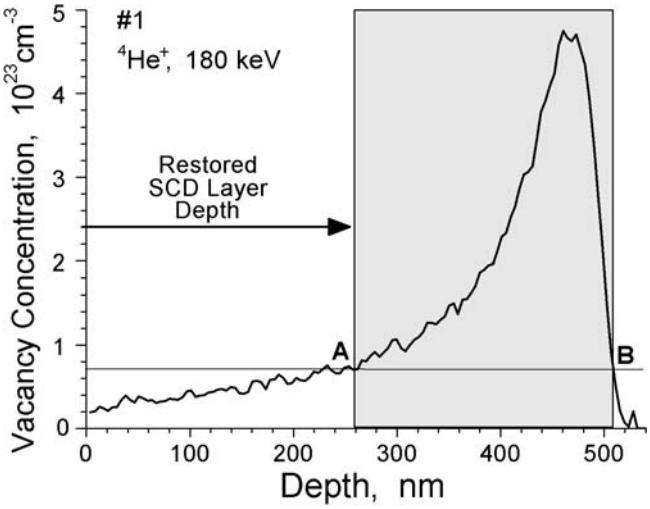

Fig. 2. Concentrations of vacancies in the SDC sample implanted with $^4He^+$ ions at an energy of 180 keV to a dose of $4 \cdot 10^{16}$ cm^{-2} (sample #1) calculated by the Monte Carlo technique. The horizontal line on the graph ($\sim 7 \cdot 10^{22}$ cm^{-3}) corresponds to the critical radiation damage. The peak on the graph determines the depth of maximum vacancy concentration. The shaded area corresponds to buried graphitized layer, and the distance AB is the graphitized layer thickness.

A typical profile of the vacancy concentration with depth for an experimental sample is shown in Fig. 2, where the graph is calculated using the model Monte Carlo simulation in SRIM software and shows the calculation of defect concentrations induced by radiation damage of specified energy and ion type in the initial structure. The constant (horizontal line, $\sim 7 \cdot 10^{22}$ cm^{-3}) on the graph corresponds to the level of graphitization, i.e., the level of critical damage at which the subsequent annealing cannot recover the diamond structure of the material and, hence, leads to the formation of a graphitized layer in the region of maximum radiation damage.

The Monte Carlo calculations performed for diamond implanted with 180 keV $^4He^+$ ions (sample #1, see Fig. 2 and Table 2) show that vacancies are predominantly concentrated (40% of the total amount) in the ∼80 nm thick layer at a depth of ∼450 nm; for 50 keV $^4He^+$ implanted diamonds, at a depth of ∼185 nm (sample #2); and for 350 keV $^{12}C^+$ implanted diamond, at a depth of ∼365 nm (sample #3);

see Table 2. The thickness of the graphitized layer for every sample is defined by points of intersection (A and B in Fig. 2) of the vacancy concentration curve and constant line of the critical damage level (see Table 2). Point A corresponds to the first diamond-graphite boundary (upper surface of graphite layer), and point B corresponds to the second graphite-diamond boundary (lower surface of graphite layer) (see Figs. 1 and 2).

The error of the presented method is about 10%. For more precise measurements of the buried graphitized layer depth and, hence, the thickness of the restored diamond layer, an additional research such as ellipsometric analysis could be done [35]. Moreover, the high quality and uniform thickness of the restored diamond layer allows one to use methods based on interferometry. Characterization of radiation damage and graphitization of diamonds could also be done by methods of optical spectroscopy (optical absorption) and measurements of "swelling" volume (see Fig. 1) [33].

2.3. Surface of the Samples

We studied the film surface (shown in Fig. 3) from the initial surface side by atomic force microscopy (AFM). Measurements were performed using a Solver Pro (NT-MDT Co.) microscope in the contact mode of surface scanning. According to the AFM data, the root-mean-square roughness of the film was 1.18 nm.

As we can see in the AFM image, nanoscale grooves that remained after treatment can be clearly observed on the ultrathin film surface. The wave-type grooves of plastic deformation is evidence of the well-done mechanical polishing of the surface. The microscale defect that can be clearly seen in the center of the AFM image is a chip and is the unavoidable result of peculiarities of mechanical treatment.

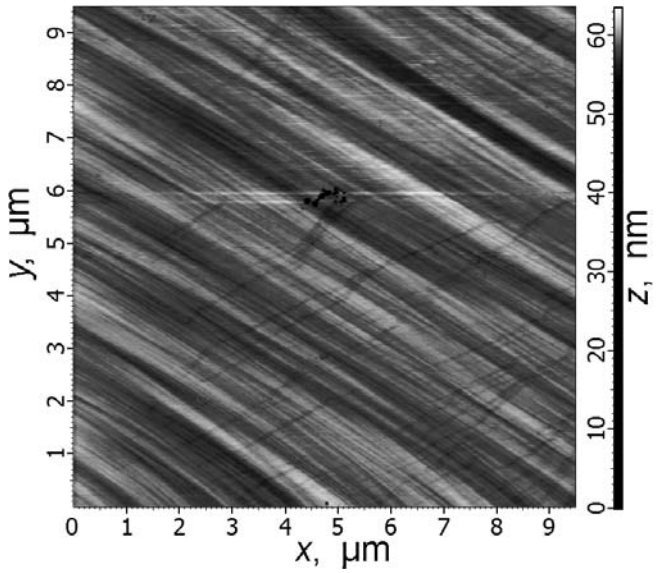

Fig. 3. A 9.5×9.5 μm AFM image of the surface of the submicron single-crystal diamond films implanted with $^4He^+$ ions at an energy of 50 keV to a dose of 2.5×10^{16} cm^{-2} (sample #2) in two-dimensional view. Horizontal and vertical axes are given in μm, and the gradient scale, in nm.

3. Experimental

The experimental setup for investigating the nonlinear optical properties of submicron diamond films is shown in Fig. 4. The source of excitation was a nanosecond pulsed Cr_3^+:Al_2O_3 (ruby) laser (wavelength 694.3 nm, pulse duration 20 ns, maximum energy 0.3 J, spectral width 0.015 cm^{-1}). Plane polarized radiation was emitted in a nearly single axial mode (divergence $3.5 \cdot 10^{-4}$ rad). Good repeatability of the single laser pulse was achieved by laser operation at constant power near the threshold at regular intervals with the ruby rod at a constant temperature.

The laser beam was focused by lenses with different focal lengths (from 3 to 10 cm) on the surface of the sample (family of crystallographic planes (110) in diamond). The angle of incidence changed from 30° to 60°. Scattered light was registered at the mirror angle. All experiments were performed under the laser-damage threshold conditions. During the experiments, we measured the spectral and intensity characteristics of the scattered light beam.

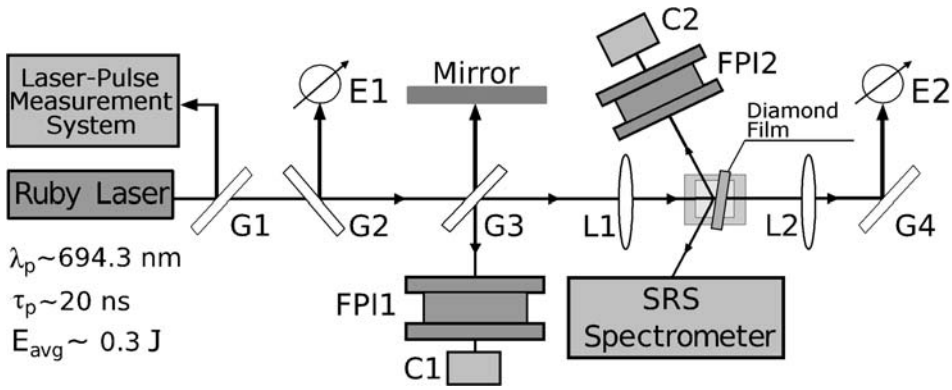

Fig. 4. Experimental setup with ruby laser, glass plates G1, G2, G3, and G4, calibrated photodiodes for scattered light energy measurements E1 and E2, reflecting mirror, Fabry–Pérot interferometers for spectral measurements FPI1 and FPI2, CCD cameras C1 and C2, lenses L1 and L2, diamond film – submicron single crystal diamond film sample, and a SRS spectrometer consisting of an FSD-8 minispectrometer with a fiber-optic input, and a measurement system of laser-light parameters.

A Fabry–Pérot interferometer (FPI) with a range of dispersion 0.7143 cm^{-1} was used for fine spectral structure registration (see Fig. 4). The fine structure of the radiation reflected from the sample at the angle of incidence and propagating towards the pump beam (in the backward direction) was measured simultaneously. Under the experimental conditions, in the backward directions no additional spectral components were registered. For the light reflected at mirror angle, additional spectral components appeared when a certain threshold value was exceeded. The pump threshold of registration was defined as 0.01 GW/cm^2. The maximum conversion efficiency of the laser light into SLFRS was 40%. The high conversion efficiency and stimulated character of the scattering is direct evidence of efficient phonon-mode excitation.

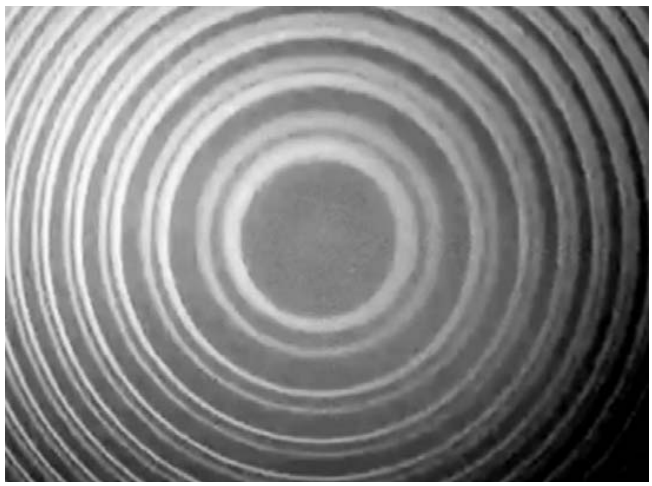

Fig. 5. Fabry–Pérot spectrum of the radiation scattered on the submicron single-crystal diamond film implanted with light ions (dispersion range 0.7143 cm^{-1}). The depth of the upper boundary of the graphitized layer of the sample is 365 nm (sample #3).

In Fig. 5, we show the SLFRS spectrum of light scattered on the submicron single crystal diamond film implanted with 350 keV $^{12}C^+$ ions.

We registered SLFRS in samples #2 and #3. The line width and divergence of SLFRS were near to the corresponding values of the exciting laser light. The SLFRS frequency shift was changed from 9 GHz for a graphitized layer with a thickness of 84 nm and a burial depth of 185 nm in sample #2 to 7.8 GHz for a graphitized layer with a thickness of 100 nm and a burial depth of 365 nm in sample #3 (see Table 3).

Phonon mode frequency is defined by the morphology of the sample consisting of the buried graphitized and diamond layers. The value of the SLFRS spectral shift (which corresponds to the excited phonon-mode frequency) decreases with increase in the structure thickness.

Table 3. SLFRS Frequencies Observed in the Submicron Diamond-Graphite-Diamond Films and Related Geometric Parameters of Experimental Samples.

Sample	Restored SCD layer depth h, nm	Graphitized layer thickness AB, nm	SLFRS frequency shift, cm^{-1}	SLFRS frequency shift, GHz
#2	185	84	0.30±0.03	9
#3	365	100	0.26±0.03	7.8

For all samples investigated, the spectral measurements were realized in a wide spectral range (from 400 to 900 nm) for radiation reflected from the sample at the angle of incidence and propagating towards the pump beam. For sample #1, we registered stimulated Raman scattering (SRS spectrometer in Fig. 4). The typical SRS spectrum observed in a submicron single-crystal diamond film implanted with 180 keV $^4He^+$ ions (sample #1) is shown in Fig. 6. The frequency shift of the first Stokes and anti-Stokes components was 1,332 cm^{-1}.

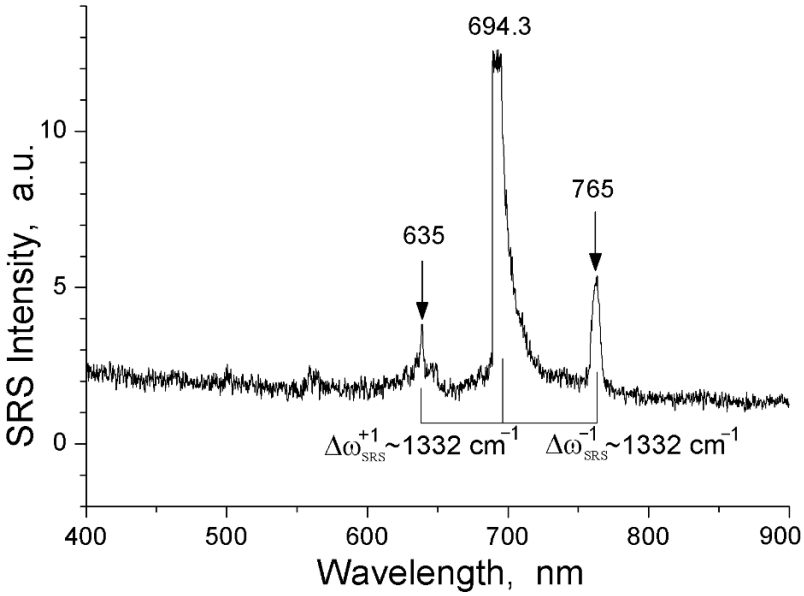

Fig. 6. Stimulated Raman scattering spectrum of the submicron single-crystal diamond film implanted with 180 keV $^4He^+$ ions (sample #1). The depth of the upper boundary of the graphitized layer of the sample is 450 nm.

The pump threshold for SRS was determined as 0.01 GW/cm^2. The maximum conversion efficiency of the exciting radiation into the scattered wave at given experimental conditions was close to 7%. The absence of SRS for samples #2 and #3 under the experimental conditions of excitation can be explained by the larger thickness of sample #1 and, thus, by the larger amplification.

4. Results and Discussion

In the present experiments, we studied stimulated Raman scattering and low-frequency Raman scattering in the stimulated regime in a set of samples of diamond-graphite-diamond heterostructures with different depths of the restored SCD layer (185–365 nm) and a graphitized layer thickness of 84–100 nm.

The excitation of the coherent phonon mode at a frequency of several GHz is a result of nonlinear interaction of high-power nanosecond laser pulses with samples of SCD films with a built-in graphitized layer. Coherent phonon generation has been observed earlier in similar heterostructures (submicron SCD film implanted with 350 keV $^{12}C^+$ ions) with a single graphitized layer under picosecond laser excitation and was treated as a thermoelastic response to photoexcitation arising in the buried graphitized

layer [36,37]. The physical mechanism of the observed phenomena can be considered as the scattering of a high-power laser light wave on the eigenvibration of an elastic graphitized layer in a solid SCD medium. A specific feature of the sp^2-carbon structure is the arrangement of atoms in the absence of long-range order [34]. The contrast in elastic properties and sound velocity in the diamond and the graphitized layer leads to the strictional absorption in the soft graphitized structure with further re-emitting on the shifted SLFRS frequency. Due to the optically smooth SCD diamond-graphitized layer boundary, the diamond-graphite-diamond heterostructure works as a resonator on longitudinal acoustic modes.

5. Summary

Our experiments demonstrated the availability of submicron SCD films with a built-in graphitized layer for purposes of nonlinear optics, namely, for effective generation of stimulated Raman and low frequency Raman scattering. Highly-efficient coherent phonon generation takes place under its excitation with nanosecond laser pulses.

Ion implantation of submicron single-crystal diamond films together with subsequent annealing allowed us to produce graphitized buried layers and high quality single- crystal diamond layers of specific nanosize thickness, matching the criteria of compatibility and scalable reproductive technology. Submicron single-crystal diamond films with a built-in graphitized layer can be used as Raman active media for spectroscopic and environmental applications.

Acknowledgments

We are grateful to Andrey Klokov for valuable discussion of the results. This work was supported by the Russian Foundation for Basic Research under Projects Nos. 16-32-60026 and 15-02-02875.

References

1. T. Popmintchev, M.-C. Chen, P. Arpin, et al., *Nature Photon.*, **4**, 822 (2010).
2. J. A. Brant, D. Clark, Y. S. Kim, and J. A. Aitken, *Chem. Mater.*, **26**, 3045 (2014).
3. P. Liu, R. Yen, and N. Bloembergen, *IEEE J. Quantum Electron.*, **14**, 574 (1978).
4. I. Wilke and S. Sengupta, *Opt. Sci. Eng.*, **131**, 41 (2007).
5. S. Albin, A. D. Cropper, L. C. Watkins, et al., *Opt. Eng.*, **28**, 283281 (1989).
6. A. H. Piracha, K. Ganesan, D. W. Lau, et al., *Nanoscale*, **8**, 6860 (2016).
7. W. Zhu, H. S. Kong, J. T. Glass, et al., "Optical applications of diamond," in: R. F. Davis (Ed.), *Diamond Films and Coatings: Development, Properties, and Applications*, Noyes Publications, New Jersey (1993), p. 244.
8. H. Nakahata, S. Fujii, K. Higaki, et al., *Semicond. Sci. Technol.*, **18**, S96 (2003).
9. B. Khanaliloo, H. Jayakumar, A. C. Hryciw, et al., *Phys. Rev. X*, **5**, 041051 (2015).
10. M. K. Zalalutdinov, M. P. Ray, D. M. Photiadis, et al., *Nano Lett.*, **11**, 4304 (2011).
11. D. Ho (Ed.), *Nanodiamonds. Applications in Biology and Nanoscale Medicine*, Springer, New York (2010).
12. M. J. Burek, N. P. de Leon, B. J. Shields, et al., *Nano Lett.*, **12**, 6084 (2012).
13. V. P. Popov, A. K. Gutakovskii, V. A. Antonov, et al., *Int. J. Nanotech.*, **12**, 226 (2015).

14. R. S. Balmer, J. R. Brandon, S. L. Clewes, et al., *J. Phys. Cond. Matter*, **21**, 364221 (2009).
15. I. Aharonovich, J. C. Lee, A. P. Magyar, et al., *Adv. Mater.*, **24**, OP54 (2012).
16. B. A. Fairchild, P. Olivero, S. Rubanov, et al., *Adv. Mater.*, **20**, 4793 (2008).
17. S. Ohmagari, H. Yamada, H. Umezawa et al., *Diamond Relat. Mater.*, **48**, 19 (2014).
18. M. Schwander and K. Partes, *Diamond Relat. Mater.*, **20**, 1287 (2011).
19. A. V. Khomich, R. A. Khmelnitskii, X. Hu, et al., *J. Appl. Spectrosc.*, **80**, 707 (2013).
20. M. V. Tareeva, V. A. Antonov, V. P. Popov, et al., *Bull. Lebedev Phys. Inst.*, **44**, 210 (2017) .
21. A. A. Kaminskii, R. J. Hemley, J. Lai, et al., *Laser Phys. Lett.*, **4**, 350 (2007).
22. E. Duval, A. Boukenter, and B. Champagnon, *Phys. Rev. Lett.*, **56**, 2052 (1986).
23. N. V. Tcherniega and A. D. Kudryavtseva, *J. Surf. Invest. X-Ray, Synchrotron Neutron Technol.*, **3**, 513 (2009).
24. M. V. Tareeva, V. S. Gorelik, A. D. Kudryavtseva, and N. V. Chernega, *Bull. Lebedev Phys. Inst.*, **37**, 331 (2010).
25. N. V. Tcherniega, M. I. Samoylovich, A. D. Kudryavtseva, et al., *Opt. Lett.*, **35**, 300 (2010).
26. N. V. Tcherniega, K. I. Zemskov, V. V. Savranskii, et al., *Opt. Lett.*, **38**, 824 (2013).
27. R. A. Khmelnitsky, V. A. Dravin, A. A. Tal, et al., *Nucl. Instrum. Methods Phys. Res. B: Beam Interact. Mater. Atoms*, **304**, 5 (2013).
28. H. J. McSkimin and P. Andreatch Jr., *J. Appl. Phys.*, **43**, 2944 (1972).
29. S. A. Solin and A. K. Ramdas, *Phys. Rev. B*, **1**, 1687 (1970) .
30. A. M. Zaitsev, *Optical Properties of Diamond. A Data Handbook*, Springer-Verlag, Berlin, Heidelberg (2001).
31. A. K. McQuillan, W. R. L. Clements, and B. P. Stoicheff, *Phys. Rev. A*, **1**, 628 (1970).
32. R. S. Sussmann, G. A. Scarsbrook, C. J. H. Wort, and R. M. Wood, *Diamond Relat. Mater.*, **3**, 1173 (1994).
33. A. V. Khomich, R. A. Khmelnitskiy, V. A. Dravin, et al., *Phys. Solid State*, **49**, 1661 (2007).
34. E. K. Nshingabigwi, T. E. Derry, S. R. Naidoo, et al., *Diamond Relat. Mater.*, **49**, 1 (2014).
35. A. V. Khomich, V. I. Kovalev, E. V. Zavedeev, et al., *Vacuum*, **78**, 583 (2005).
36. A. Klokov, A. Sharkov, V. Vershkov, et al., *Abstracts of the 19th International Conference on Photoacoustic and Photothermal Phenomena (16–20 July 2017, Bilbao)*, p. 181.
37. A. Klokov, M. Kochiev, A. Sharkov, et al., *J. Phys. Conf. Ser.*, **278**, 012019 (2011).